Wide Compositional Range *In Situ* Electric Field Investigations on Lead-Free $Ba(Zr_{0.2}Ti_{0.8})O_3$-$x(Ba_{0.7}Ca_{0.3})TiO_3$ Piezoceramic

M. Zakhozheva,[1] L. A. Schmitt,[1] M. Acosta,[1] H. Guo,[2] W. Jo,[3] R. Schierholz,[4] H.-J. Kleebe,[1] and X. Tan[2]

[1]*Institute of Geo- and Material Sciences, Technische Universität Darmstadt, 64287 Darmstadt, Germany*
[2]*Department of Materials Science and Engineering, Iowa State University, Ames, Iowa 50011, USA*
[3]*School of Materials Science and Engineering, Ulsan National Institute of Science and Technology, Ulsan 689-798, Republic of Korea*
[4]*Institute of Energy and Climate Research: Fundamental Electrochemistry IEK-9, Forschungszentrum Jülich, 52425 Jülich, Germany*

(Received 25 November 2014; published 24 June 2015)

The evolution of ferroelectric domains in the lead-free $Ba(Zr_{0.2}Ti_{0.8})O_3$-$x(Ba_{0.7}Ca_{0.3})TiO_3$ (abbreviated as BZT-xBCT) piezoelectric ceramic is investigated *in situ* under an applied electric field using transmission electron microscopy (TEM). Poling-induced, reversible, transformation from a multidomain to a single-domain state is monitored for a large variety of compositions. For all studied materials, this transformation occurs with the appearance of an intermediate nanodomain state at moderate poling fields. According to our results, under high poling fields, a single-domain state vanishes and multiple domains reappear within the grains. Upon further cycling, switching between two different multidomain states occurs. For all BZT-xBCT compositions that we investigate, no sign of the electric-field-induced structural changes is detected using the selected area electron-diffraction (SAED) patterns, which are devoid of the reflection splitting or any detectable changes during electrical poling. The extrinsic contribution to the piezoelectric properties is found to dominate in the BZT-xBCT piezoceramic.

DOI: 10.1103/PhysRevApplied.3.064018

I. INTRODUCTION

Piezoelectric ceramics are a class of materials that produce charge when a mechanical stress is applied to them and vice versa. These materials are used in numerous applications such as sensor and actuator devices. Because of its superior electromechanical properties, a perovskite lead-based piezoceramic $Pb(Zr_xTi_{1-x})O_3$ (PZT) remains the material of choice and has been for the last fifty years [1]. However, because of the toxicity of Pb and PbO, environmental regulations in many countries initiated a search for suitable lead-free substitutes for PZT [2]. Numerous lead-free systems containing $BaTiO_3$, $Bi_{0.5}Na_{0.5}TiO_3$, $Bi_{0.5}K_{0.5}TiO_3$, $BaZr_xTi_{1-x}O_3$, $Ba_{1-x}Ca_xTiO_3$, $(K_{0.5}Na_{0.5})NbO_3$, etc., were investigated during the last few decades [3–9]. Nevertheless, piezoelectric and ferroelectric properties in most Pb-free piezoceramics are still inferior to PZT [4,10,11]. Therefore, searching for a new type of lead-free piezoelectric material for various environment-friendly commercial applications is of great necessity.

In the recent past, much attention was given to the BZT-xBCT perovskite ferroelectric, first published by Liu and Ren [12], due to its enhanced piezoelectric properties [13–18]. According to Liu and Ren, the phase diagram of the BZT-xBCT pseudobinary system contains paraelectric cubic (C), ferroelectric rhombohedral (R), and ferroelectric tetragonal (T) phases separated by a temperature-dependent morphotrophic phase boundary (MPB), which is more precisely named as a polymorphic phase transition (PPT). For the BZT-0.5BCT composition, which lies on the PPT at room temperature, they observed an especially high piezoelectric coefficient ($d_{33} = 620$ pC/N). The high piezoelectricity is attributed to the fact that PPT starts from the tricritical triple point, which indicates a low-energy barrier between C, R, and T phases and therefore enables enhanced polarization rotation around the triple point [12]. The reduced free-energy anisotropy was recently calculated by a phenomenological approach and indeed a broad area of the phase diagram presents a low-energy barrier for polarization rotation, specifically around phase boundaries [19]. It should be noted that the triple point, where the paraelectric C phase coexists with ferroelectric R and T phases, is also observed for high-piezoelectric PZT and $Pb(Zn_{1/3}Nb_{2/3})O_3$–$PbTiO_3$ (PZN-PT) systems [20]. The phase diagram of BZT-xBCT is still under discussion in the literature, despite the fact that many investigations support a phase diagram initially designed by Liu and Ren [13,21]. For example, numerous investigations show an area around PPT, where the coexistence of R and T phases is observed [22–25], whereas other studies propose the presence of an intermediate orthorhombic (O) phase between R and T and a phase-convergence region [26–28].

As mentioned above, enhanced piezoelectric performance is observed for the PPT composition BZT-0.5BCT [12,14,15]. Moreover, at this composition, miniaturization of domains was also reported [22,29]. Gao *et al.* observed the presence of nanosized domains, which formed a

hierarchical domain structure for BZT-0.5BCT [22,29]. With a convergent-beam electron-diffraction technique, they showed a coexistence of *T* and *R* crystal symmetries for BZT-0.5BCT and suggested that enhanced polarization rotation between *T* and *R* phases at nanoscale is responsible for the strong piezoelectric properties of BZT-0.5BCT [22,29]. It should be emphasized that such a nanoscale, hierarchical, domain structure is also observed in lead-containing materials with high piezoelectric activity, such as $Pb(Mg_{1/3}Nb_{2/3})O_{3-x}PbTiO_3$ [30–32]. The main contribution to the high piezoelectric properties in BZT-0.5BCT was suggested to be the result of the domain-wall displacement (extrinsic contribution) [17]. This is in agreement with a report by Zhukov *et al.* [33], who showed increased domain-wall motion near PPT as a result of a minimum energy barrier for polarization rotation between two ferroelectric phases. However, our recent *in situ* TEM studies showed a high extrinsic effect in BZT-0.3BCT composition as well [34], which has a rhombohedral crystal symmetry [12,15,26]. Hence, a high extrinsic contribution to the piezoelectric response is not a unique feature of PPT compositions. In fact, recent work suggests that the elastic softening observed at the compositions around PPT provides a major contribution to the piezoelectric activity [19,35,36]. This, in turn, could lead to stress relief and, hence, allow for enhanced domain switching.

Using *in situ* TEM, recent investigations show the formation of a unique single-domain state in BZT-0.5BCT during electrical poling [36,37]. This single-domain-state formation was associated with enhanced piezoelectric properties in the system. Nevertheless, such a single-domain state was also reported for the rhombohedral BZT-0.3BCT [34] and, therefore, is not an exclusive characteristic of the PPT composition.

Most of these studies concentrate on the BZT-*x*BCT composition around the PPT region [17,29,36,37], because of its outstanding properties. However, to fully understand the structure-property relationship, the domain-morphology evolution should be investigated in a broad compositional range. In this article, we report a composition-dependent *in situ* electric-field-induced microstructure evolution in the lead-free BZT-*x*BCT system. Finally, strain and polarization measurements as a function of electric field are contrasted with the *in situ* electric-field TEM findings.

II. EXPERIMENT

Piezoelectric ceramics $Ba(Zr_{0.2}Ti_{0.8})O_3$-$x(Ba_{0.7}Ca_{0.3})TiO_3$ (with $x = 0.3$, 0.32, 0.4, 0.45, 0.52, and 0.6) are produced via a conventional solid-state-reaction method from oxides and carbonate powders of $BaCO_3$ (purity 99.8%), ZrO_2 (purity 99.5%), TiO_2 (purity 99.6%), and $CaCO_3$ (purity 99.5%). The powders are calcined at 1300 °C for 2 h and then sintered at 1500 °C for 2 h. Detailed information on sample synthesis is given elsewhere [15,33].

Room-temperature strain and polarization measurements are performed in a modified Sawyer-Tower setup with a measurement capacitance of 10 μF. The circuit is coupled with an optical displacement sensor (Philtec, Annapolis, MD, USA) to measure displacements. A triangular wave of 3 kV/mm and 1 Hz is used as the input signal.

The theoretical analysis of reflection splitting in SAED patterns for rhombohedral and tetragonal ferroelectric domains in the BZT-*x*BCT system is performed with MATLAB (MathWorks, Nattick, MA, USA), using the lattice parameters originally reported by Liu and Ren (tetragonal, $a = 4.007$ Å and $b = 4.025$ Å; rhombohedral, $a = 4.009$ Å and $\alpha = 89.88°$) [12]. The amount of splitting (s) is defined using the following equation:

$$s = \frac{|(g_{hkl1} - g_{hkl2}) - (g_{hkl1} - g_{hkl2}) \cdot [uvw]|}{|g_{hkl}|}, \quad (1)$$

where $[uvw]$ is a vector, parallel to the zone axis; and g_{hkl1} and g_{hkl2} are a pair of reflections with the largest splitting for a certain zone axis [38]. Detailed information on reflection-splitting calculations is given in Ref. [38].

For TEM studies, specimens are prepared by a conventional method of mechanical thinning, polishing, dimpling, and ion milling [34]. Gold electrodes are sputtered on top of the specimens and contacted with Pt wires to the *in situ* electric-field holder (Gatan, model 646). *In situ* TEM experiments are performed using a CM30 instrument (FEI, Eindhoven, Netherlands) operated at 200 kV and 250 kV. Maximum applied voltage is 500 V.

III. RESULTS AND DISCUSSION

In Figs. 1(a)–1(c), ferroelectric hysteresis loops of BZT-*x*BCT ($x = 0.30$, 0.52, 0.60) ceramic at room temperature are depicted. From the *P*-*E* hysteresis loops, the ferroelectric properties (saturation polarization, remanent polarization, and coercive field) for a wide range of BZT-*x*BCT ($x = 0.30$, 0.32, 0.40, 0.45, 0.52, 0.60) are examined as a function of composition. The maximum values of saturation polarization ($P_s \sim 18.80$ μC/cm^2) and remanent polarization ($P_r \sim 12.25$ μC/cm^2) are observed for BZT-0.45BCT [Figs. 2(a) and 2(b)]. The coercive field (E_c) increases with increasing Ca content but the coercive field has a small decrease for BZT-0.4BCT [Fig. 2(c)]. The coercive field for rhombohedral BZT-*x*BCT is much lower than that for the tetragonal compositions.

Maximum and remanent strain (S_{max} and S_r, respectively) are also measured from bipolar strain loops [Figs. 1(d)–1(f)] for all compositions [Figs. 2(d) and 2(e)]. Increased values of S_{max} and S_r are observed for the BZT-0.4BCT and BZT-0.52BCT compositions, which are close to the PPT of the phase diagram [15,26].

According to calculations of the reflection splitting, rhombohedral 71° and 109° domains with walls in {100} and {110} planes, respectively (nomenclature is

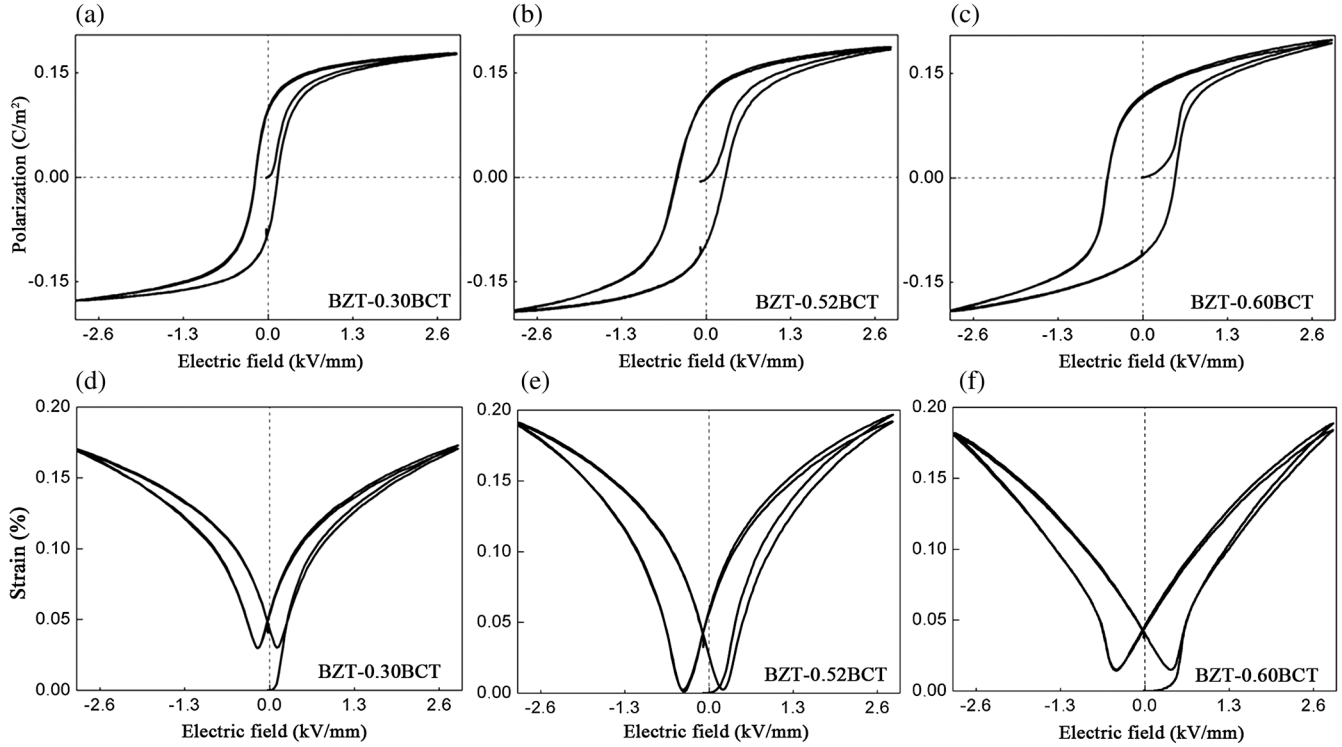

FIG. 1 (a)–(c) Room temperature *P-E* hysteresis loops. (d)–(f) Room temperature bipolar *S-E* loops of BZT-0.3BCT, BZT-0.52BCT, and BZT-0.6BCT, respectively.

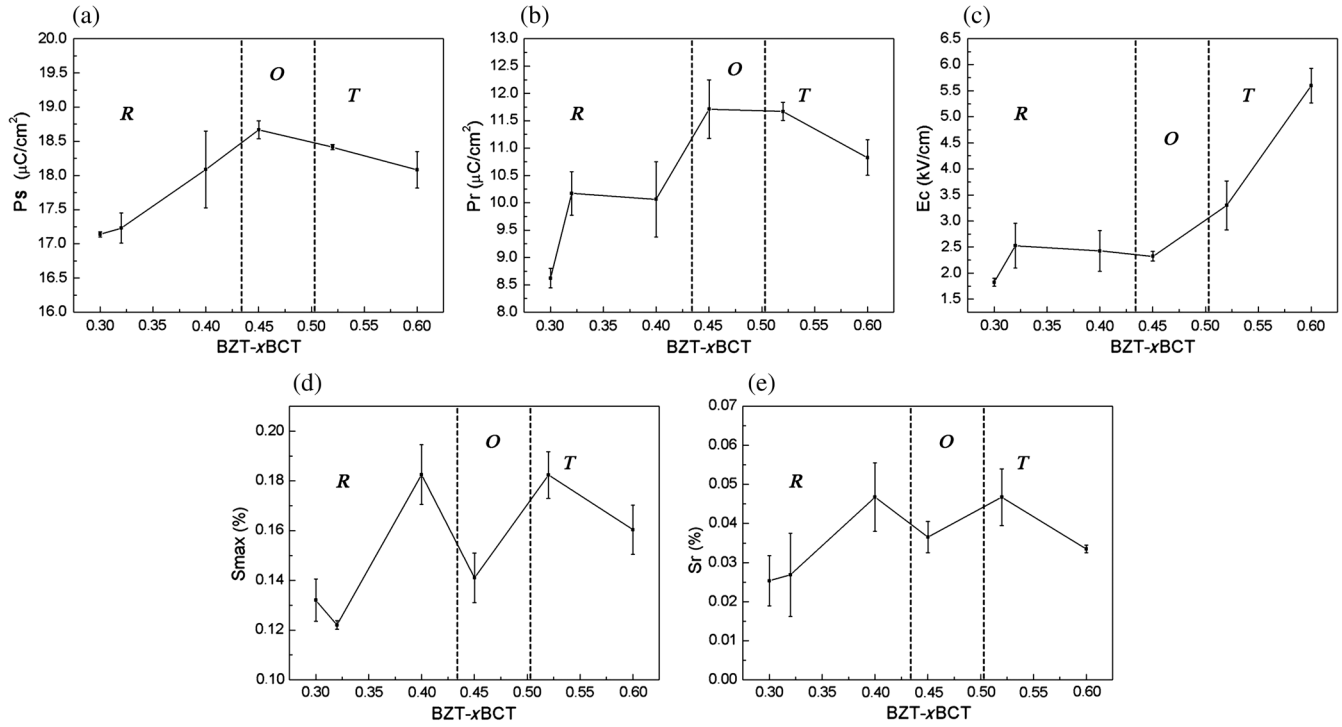

FIG. 2. (a) Saturation polarization P_s. (b) Remanent polarization P_r. (c) Coercive field E_c. (d) Maximum strain $S_{\max}$. (e) Remanent strain S_r as a function of composition. Dashed lines indicate phase boundaries between $(R\text{-}O)$ and $(O\text{-}T)$ phases.

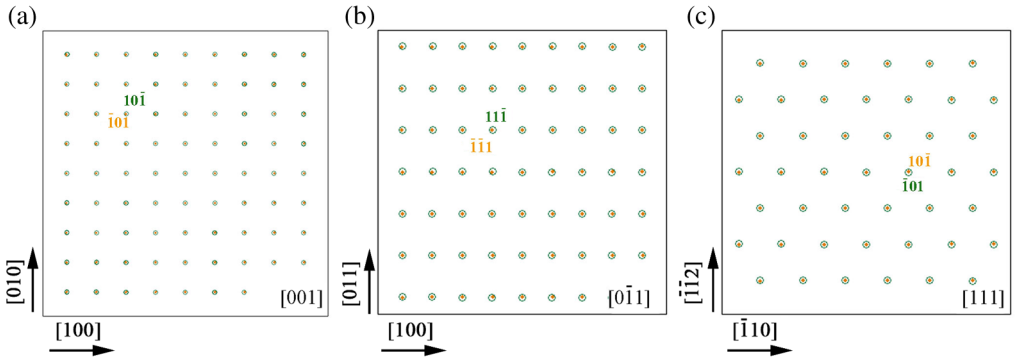

FIG. 3. Calculated SAED patterns for tetragonal 90° domains along the (a) [001] zone axis. (b) [0$\bar{1}$1] zone axis. (c) [111] zone axis. Reflections, which are used for calculation of the parameter s, are indicated (green and orange).

from Ricote *et al.* [39]), produce very small splitting in the SAED patterns. The largest reflection splitting, $s = 0.0024$, for rhombohedral domains occurred in [0$\bar{1}$1] zone axis for {100} domain walls and in [1$\bar{1}$0] and [1$\bar{1}$1] zone axes for {110} domain walls. The amount of reflection splitting, produced by tetragonal 90° domains, achieved its maximum, $s = 0.0079$, in the [001] crystallographic orientation. For the [0$\bar{1}$1] zone axis, the parameter s is calculated to be 0.0056; for [111] and [1$\bar{1}$1] orientation, splitting achieved the value of 0.0046. Even smaller splitting of the reflections is observed for other crystallographic orientations. Figure 3 illustrates calculated SAED patterns produced by the presence of tetragonal 90° domains along the [001], [0$\bar{1}$1], and [111] zone axes.

The domain-morphology evolution during electrical poling in BZT-0.30BCT is studied using the grain imaged along the $[1\bar{5}3]_c$ zone axis [Fig. 4]. Prior to applying an electric field, two sets of lamellar domains with an average width of 298 ± 42 nm are observed inside the grain [Fig. 4(a)]. During the initial poling, a single-domain state occurs when the electric field reaches 2.66 kV/cm [Fig. 4(b)]. The corresponding SAED patterns do not reveal any obvious splitting of the reflections or any detectable changes during electrical poling [Fig. 4(a) and 4(b), insets]. This can be attributed to very small R distortions, which result in very thin peak splitting that cannot be detected in SAED due to the resolution limit.

The remanent state after poling shows a multiple-domain configuration reappearing, similar to that observed in the virgin state [Fig. 5(a)]. A small increase in the electric field to 0.66 kV/cm leads to the miniaturization of domains to nanometer size [Fig. 5(b)]. When the electric field is raised to 1.33 kV/cm, all domain walls disappear, forming a single-domain state throughout the grain [Fig. 5(c)]. Thus, transformation from a multidomain to a single-domain state occurs with the appearance of an intermediate nanodomain state. These changes in domain morphology are observed to be reversible. The single-domain state is stable at high poling fields up to 4 kV/cm. A decrease in the poling field to 2 kV/cm leads to the formation of domain walls in the regions close to the grain boundaries [Fig. 5(d)]. Existing domains grow upon further decrease in the electric field [Fig. 5(e)] and, at zero field, the domain-wall density reaches its maximum. The domain pattern significantly changes, compared to the virgin state, which indicates the presence of a multiple-domain state with remanent polarization [Fig. 5(f)]. Nanosized domains are observed inside the lamellar microdomains at zero field after the sample is poled again [Fig. 5(f)]. During poling reversal, the domain contrast completely disappears at the nominal poling field of −2.66 kV/cm [Fig. 5(g)]. But this single-domain state is not stable at higher poling fields. New sets of domains start to form from the grain boundary when the field strength reaches a nominal value of −14 kV/cm [Fig. 5(h)]. Further

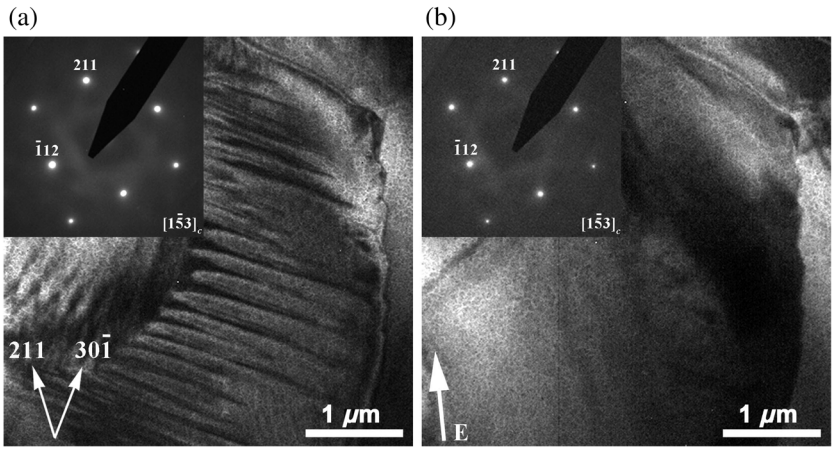

FIG. 4. *In situ* TEM bright-field images of the BZT-0.3BCT along the $[1\bar{5}3]_c$ zone axis at (a) virgin state. (b) 2.66 kV/cm. The direction of the poling field is indicated by the bright arrow on (b). In the insets, the corresponding SAED patterns are depicted.

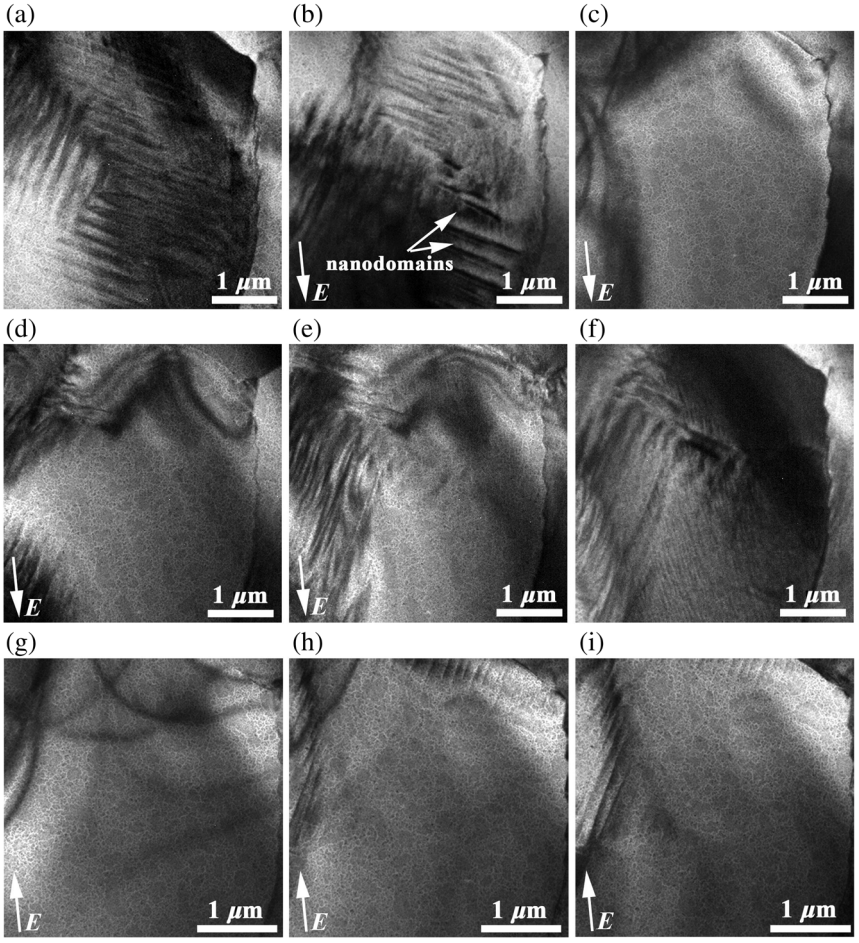

FIG. 5. *In situ* TEM bright-field images of the BZT-0.3BCT along the $[1\bar{5}3]_c$ zone axis at (a) zero field. (b) 0.66 kV/cm. (c) 1.33 kV/cm. (d) 2 kV/cm. (e) 0.66 kV/cm. (f) Zero field. (g) −2.66 kV/cm. (h) −14 kV/cm. (i) −20 kV/cm. The direction of the poling field is indicated by the bright arrows.

increase of the poling field induces the growth of the existing lamellar domains [Fig. 5(i)]. The electric-field dependence of SAED patterns for this composition shows behavior similar to SAED patterns for the reported BZT-0.3BCT [34] and BZT-0.5BCT [36], with no clear changes during the poling process, which can be related to the resolution limit of SAED.

For BZT-0.32BCT, the evolution of ferroelectric domains under an applied electric field is examined using a grain oriented along the $[1\bar{1}0]_c$ zone axis [Fig. 6]. In the virgin state, lamellar $\{110\}$ domains with an average width of around 144 ± 30 nm are observed [Fig. 6(a)]. With an increase of the poling field, the domain walls start to disappear from the regions close to the grain boundary [Figs. 6(a)–6(d)]. A transformation from a multidomain to a single-domain state occurs at the nominal poling field of 3.2 kV/cm [Fig. 6(d)]. By applying a poling field of 4.2 kV/cm, domains start to form within the grain [Fig. 6(e)]. Nucleation of new sets of micro- and nanodomains occur when the electric field is further increased [Fig. 6(f)]. The corresponding SAED patterns during the poling process are depicted in Figs. 6(g)–6(i). Neither any reflection splitting nor detectable changes during the electrical poling are observed, which is expected, considering the small distortions from our calculations.

TEM micrographs of BZT-0.4BCT during the poling process are depicted in Fig. 7. Prior to the application of an external field, thin ferroelectric domains with an average width of 50–100 nm are observed within grain imaged along the $[0\bar{1}0]_c$ zone axis. These multiple domains have traces of domain walls along the [001] direction in the initial state [Fig. 7(a)]. At the nominal poling field of 1.5 kV/cm, domain contrast disappeared completely [Fig. 7(b)], indicating a transformation from multidomain to a single-domain state. Upon field removal, domain walls reappeared inside the grains. The insets in Figs. 7(a) and 7(b) show the corresponding SAED patterns. Due to the small distortions, a reflection splitting in the SAED patterns cannot be resolved.

The evolution of the domain morphology under an external electric field of BZT-0.45BCT is shown in Fig. 8. Initially, areas with nanodomain structure are visible [Fig. 8(a)] inside the lamellar domains, which have an average width of 145 ± 36 nm and are tracing along the $\langle 111 \rangle$ direction. Under an applied electric field, the density of nanodomains increases [Figs. 8(b) and 8(c)] and, at 2.66 kV/cm, a whole grain transforms into a large single domain [Fig. 8(d)]. Similar to previous cases, SAED patterns do not exhibit any significant changes with increasing poling field [insets in Figs. 8(a) and 8(d)].

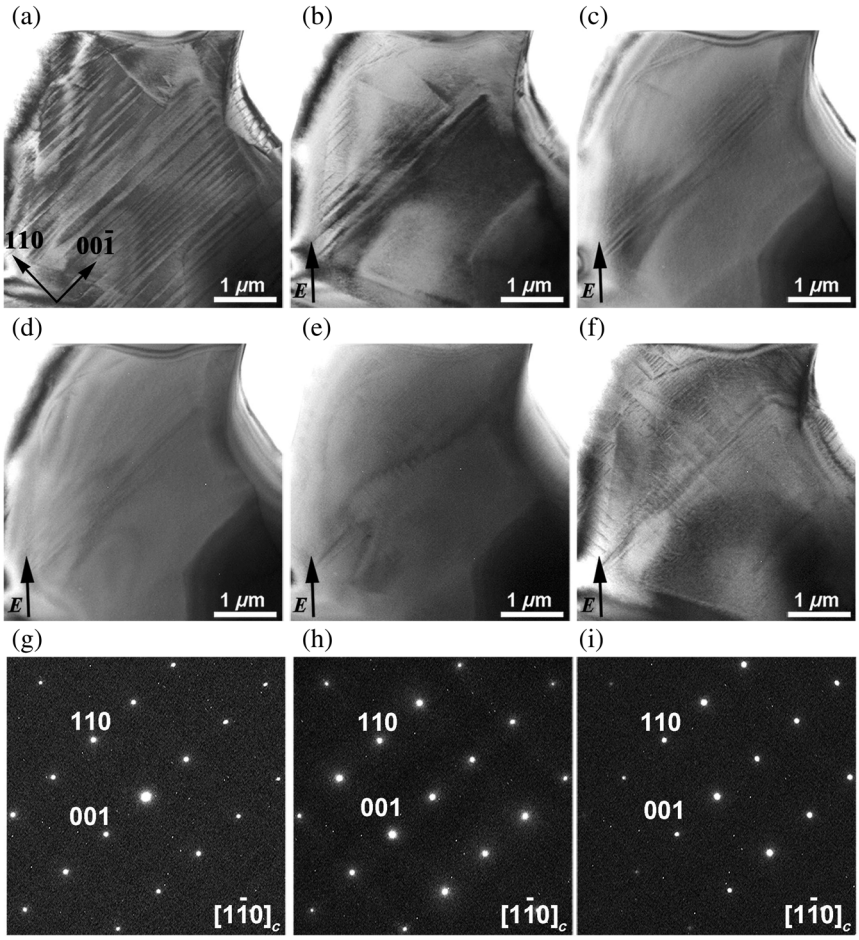

FIG. 6. *In situ* TEM bright-field images of the BZT-0.32BCT along the $[1\bar{1}0]_c$ zone axis at (a) virgin state. (b) 1.48 kV/cm. (c) 2 kV/cm. (d) 3.2 kV/cm. (e) 4.2 kV/cm. (f) 5 kV/cm. The direction of the poling field is indicated by the dark arrows. Corresponding SAED patterns at (g) virgin state. (h) 2 kV/c. (i) 5 kV/cm.

Figure 9 shows field-induced domain switching in BZT-0.52BCT. Prior to applying an electric field, a hierarchical domain structure with an average domain width of 128 ± 12 nm is observed inside grain that is imaged along the $[1\bar{1}0]_c$ zone axis [Fig. 9(a)]. When the field reaches 1.66 kV/cm, a single-domain state is formed [Fig. 9(b)]. When the electric field is further increased, the single-domain state transforms to a multidomain state again [Figs. 9(c) and 9(d)]. Lamellar microdomain structure and miniaturized nanodomains appear at the nominal field strength of 5.83 kV/cm [Fig. 9(c)]. When the electric field is raised to 7.5 kV/cm, only lamellar domain walls with traces along the $\langle 111 \rangle$ direction are present inside the grain. No visible changes in the corresponding SAED patterns during the electrical poling are observed [Fig. 9, insets].

It should be emphasized that, in this composition, a single-domain state does not appear while diminishing the electric field after the multiple-domain state is achieved,

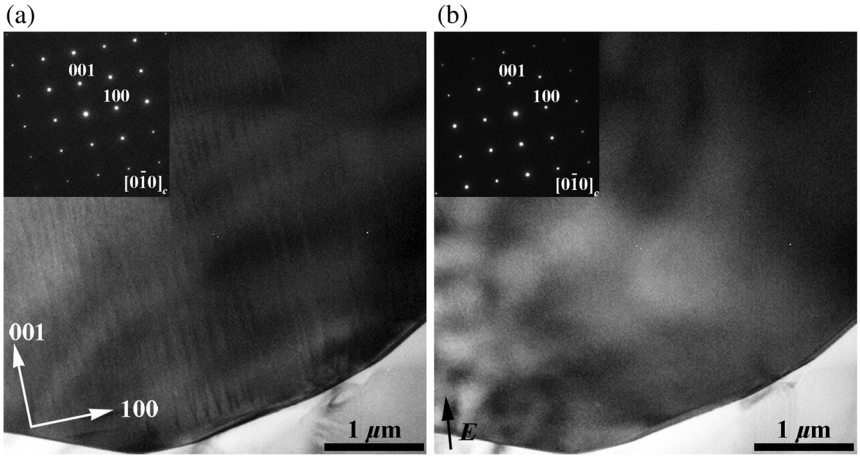

FIG. 7. *In situ* TEM bright-field images of the BZT-0.40BCT along the $[0\bar{1}0]_c$ zone axis at (a) virgin state. (b) 1.5 kV/cm. The direction of the poling field is indicated by the dark arrow on (b). In the insets, the corresponding SAED patterns are depicted.

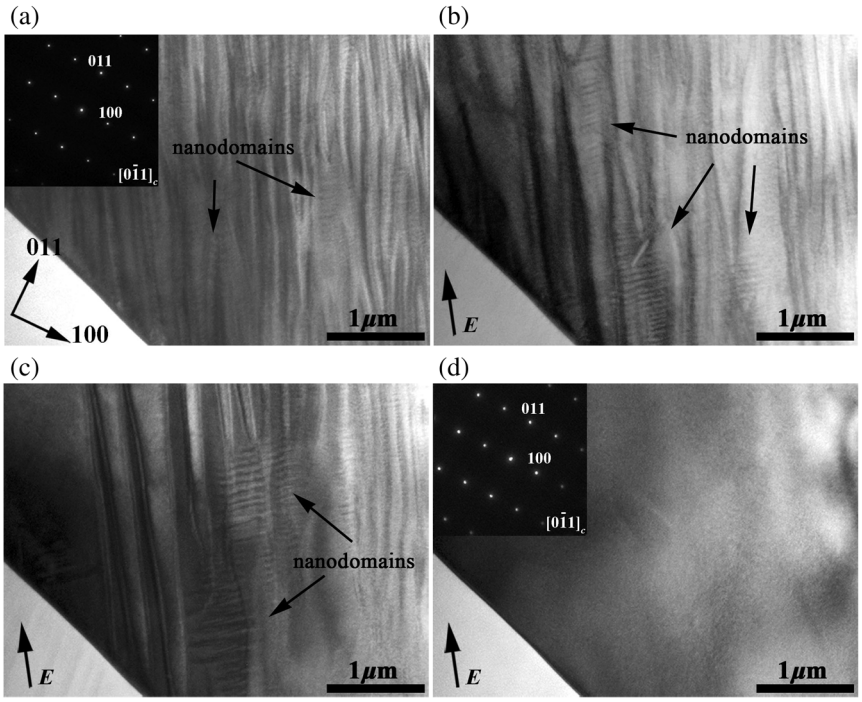

FIG. 8. *In situ* TEM bright-field images of the BZT-0.45BCT along the $[0\bar{1}1]_c$ zone axis at (a) zero field. (b) 1.25 kV/cm. (c) 2.08 kV/cm. (d) 2.66 kV/cm. The direction of the poling field is indicated by the dark arrows. In the insets, the corresponding SAED patterns are depicted.

which is similar to the observations in the PPT composition of BZT-0.5BCT [36,37]. When the applied electric field is completely removed, a hierarchical domain structure is observed inside the grain [Fig. 10(a)]. Figures 10(b)–10(d) show the evolution of a domain configuration during the repoling process, when the external electric field is reversed in polarity. At about 6.5 kV/cm, a single-domain state is achieved. However, this single-domain state transforms into a multidomain state within few seconds at the same field strength. Such a phenomenon, indicating the instability of the single domain state, is also consistent with the observations in BZT-0.5BCT [37], where multidomains emerge from the grain boundary by maintaining the poling field at the single-domain state.

For BZT-0.6BCT, a grain oriented along $[1\bar{1}2]_c$ zone axis is used to analyze the domain-structure evolution during electrical poling [Fig. 11]. At the virgin state, lamellar domain walls are observed, which trace along the ⟨110⟩

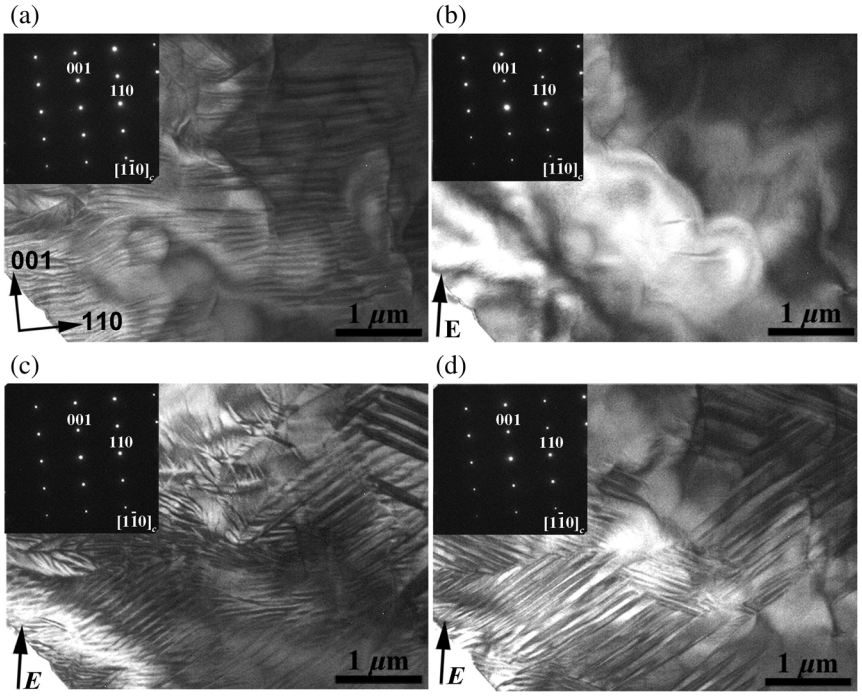

FIG. 9. *In situ* TEM bright-field images of the BZT-0.52BCT along the $[1\bar{1}0]_c$ zone axis at (a) virgin state. (b) 1.66 kV/cm. (c) 5.83 kV/cm. (d) 7.5 kV/cm. The direction of the poling field is indicated by the dark arrows. In the insets, the corresponding SAED patterns are depicted.

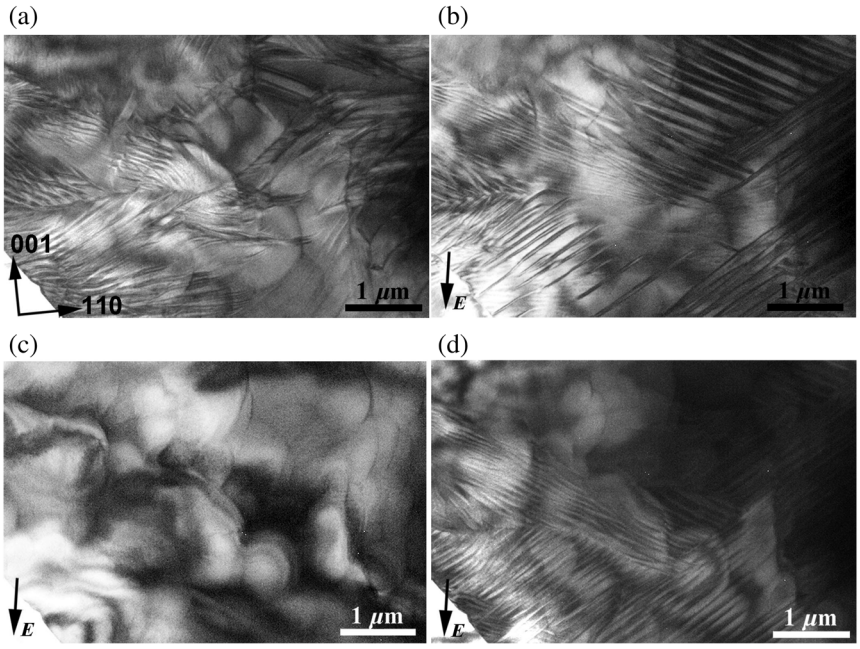

FIG. 10. *In situ* TEM bright-field images of the BZT-0.52BCT along the $[1\bar{1}0]_c$ zone axis at (a) zero field. (b) −5.83 kV/cm. (c) −6.5 kV/cm. (d) −6.5 kV/cm after 10 s. The direction of the poling field is indicated by the dark arrows.

direction [Fig. 11(a)]. The average domain width at the initial state is determined to be 173 ± 41 nm. No changes in the domain morphology are detected up to the nominal poling field of 7.66 kV/cm. When the electric field achieved the value of 8.66 kV/cm, the domains with a hierarchical structure and nanodomains are formed across the grain [Figs. 11(a) and 11(b)]. During the first half cycle, a single-domain state does not appear even at the poling field of 12 kV/cm. After poling, in the remanent state, nanometer-sized ferroelectric domains are still visible [Fig. 11(c)]. During poling reversal, domain morphology slightly changes, but the multidomain structure is present even at −8.66 kV/cm [Fig. 11(d)]. It should be noted that, for this composition, the transformation to a single-domain state occurs at an electric field of 20 kV/cm. Because the resolution is not sufficient, SAED patterns are devoid of reflection splitting and no detectable changes are visible during electrical poling [Figs. 11(b) and 11(c), insets).

For all studied BZT-*x*BCT compositions, the splitting of the reflections is not detected in SAED patterns. The reflection splitting, which is an indication of twinning, occurs as a result of the ferroelastic distortions of the unit cell due to mismatch of the crystal lattice of two adjacent domains (except 180° domains) [40,41]. However, for all

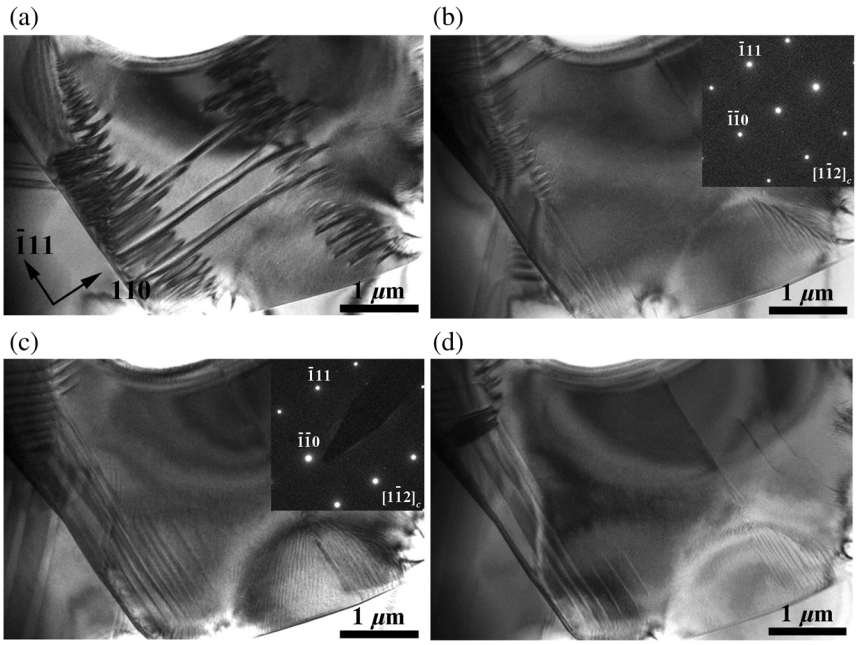

FIG. 11. *In situ* TEM bright-field images of the BZT-0.60BCT along the $[1\bar{1}2]_c$ zone axis at (a) virgin state. (b) 8.66 kV/ cm. (c) zero field. (d) −8.66 kV/cm. In the insets, the corresponding SAED patterns are depicted.

studied BZT-xBCT compositions, the distortions are so small that the splitting of the reflections cannot be detected in the SAED patterns due to saturation limit of the CCD camera. However, this limitation can be overcome by means of a high-dynamic-range (HDR) electron-imaging technique, as reported by Evans and Beanland [42]. This technique enables one to enhance the intensity of weak reflections without increasing in the intensity of strong reflections. HDR analysis is left as future work, because it can give further insights into the intrinsic contributions to the piezoelectric activity of the BZT-xBCT.

According to the results of the domain-size analysis for all studied BZT-xBCT compositions, lamellar domains in the submicron range are detected. At the initial state, nanometer-sized domains are present within domain lamellas for BZT-0.45BCT, which is located around the PPT [15,26]. Similar results are obtained by Gao *et al.* [22,29]; they observed a miniaturized nanodomain structure inside microdomains for PPT composition BZT-0.5BCT [15,26], which exhibits enhanced piezoelectric properties. The reduction in the domain size to the nanoscale level near the phase-transition regions is expected from classical domain theory [43]. The theory predicts that the domain width is proportional to the square root of the domain-wall energy ($D \sim \gamma^{1/2}$), which strongly decreases near the phase transition [44]. As mentioned above, areas occupied by nanodomains in BZT-0.45BCT increase with the poling field. Moreover, nanometer-sized domains form during the poling process for other compositions as well. This miniaturized nanodomain structure eases domain switching and therefore facilitates the poling process. It should be emphasized that analogous behavior is observed in previously reported $(Pb_{0.92}La_{0.08})(Zr_{0.65}Ti_{0.35})O_3$ (PLZT) [45] and PZT [46]. In the first case, switching occurred through the formation of an intermediate nanodomain state [45], while in the other case the nanodomains already existed in the initial state and responded to the electric field during the poling process [46].

A transformation from multidomain to a single-domain state for tetragonal BZT-0.6BCT composition occurs at the nominal poling field of 20 kV/cm, which is much higher than that of rhombohedral and PPT compositions. This coincides with the higher coercive fields measured when approaching T symmetry [Fig. 2(c)]. Therefore, higher fields are required to achieve a proper poling of BZT-0.6BCT, which is located deep in the tetragonal region. This result is in good agreement with the calculations of activation barrier for the nucleation of reversed domains, determined by Zhukov *et al.* [33]. According to their calculation, the minimum in activation barrier is around PPT at room temperature, indicating a facilitated domain switching for compositions around the PPT [47]. The value of the energy barrier increases for BZT-0.35BCT and achieves its maximum for BZT-0.6BCT, which has a tetragonal symmetry [33]. Consequently, enhanced polarization switching is observed around PPT compositions and is impeded for T and R compositions, which are far away from the PPT. In the present study, the maximum poling field of 20 kV/cm is applied to reach a single-domain state in BZT-0.6BCT.

Based on the results of the *in situ* electric field experiments on BZT-xBCT, the schematic domain evolution depicted in Fig. 12 is suggested. In general, with an increasing poling field, a transformation from multidomain to a single-domain state occurs in all studied compositions. This transformation is found to be reversible as the multidomain state reappears inside the grains upon field removal [Fig. 12(a)]. Formation of a single-domain state during the poling process is initially reported only for PPT-composition BZT-0.5BCT and is associated with high piezoelectric properties, together with the consideration of elastic softening [36,37]. Our previous studies show that transformation from multidomain to a single-domain state occurs under poling conditions in the rhombohedral BZT-0.3BCT [34]. In the present work, such transformation is observed in all studied materials, even in the tetragonal BZT-0.6BCT. As mentioned before, an intermediate nanodomain state

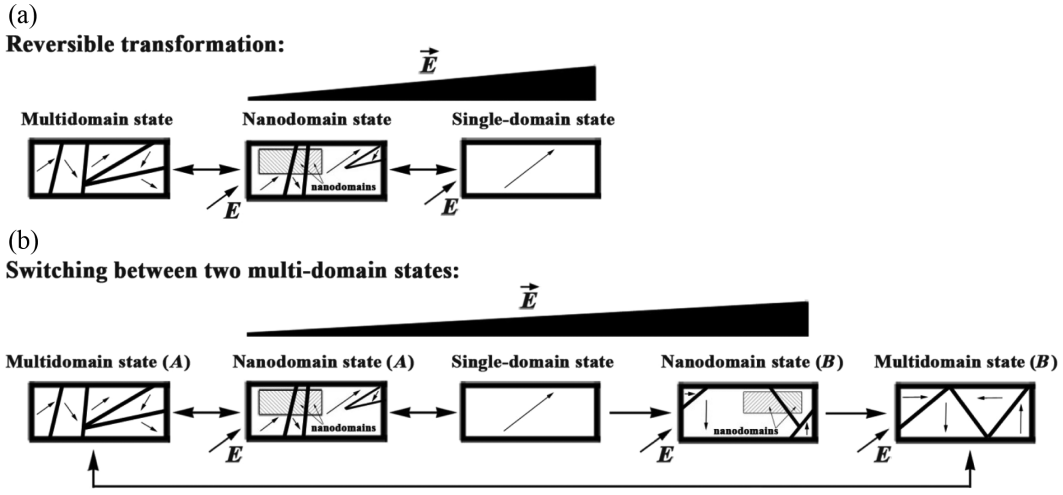

FIG. 12. Scheme of domain evolution in BZT-xBCT. (a) Reversible domain transformation. (b) Switching between two multidomain states.

appears in several grains during the poling process. The appearance of a nanodomain structure, followed by the formation of micron-sized lamellar domains, is observed during further increase in the poling field, even though the electric-field threshold value differs, depending on composition [Fig. 12(b)].

This multiple-domain formation can be related to the strain incompatibility between adjacent grains. Under high poling fields, each grain represents a single domain. With respect to the external electric field, preferred alignment of the polarization vector cannot be completely achieved within each single grain of the polycrystalline sample. Hence, a strain incompatibility between those grains and surrounding grains prevails. Consequently, transformation from a single-domain to multidomain state occurs during additional field increases. It should be noted that a single-domain state cannot be achieved during field releasing once the multidomain state is induced [Fig. 12(b)]. During the repoling process, the single-domain state appears only for BZT-0.52BCT composition and is stable only for a few seconds, suggesting that this state seems to be metastable under the studied conditions.

Because orientation of the grains relative to the electric-field vector affects the strain mechanisms in piezoceramics, different sample orientations have to be studied in order to obtain a full picture on all possible poling mechanisms in certain materials [48,49]. Results of our studies clearly demonstrate that the external electric field induces domain-wall motion in the BZT-*x*BCT system. This suggests that the strain mechanism of BZT-*x*BCT presents a high extrinsic contribution. We suggest that the miniaturized domains far away from phase boundaries may result from domain frustration due to internal stresses. This phenomenon is not currently understood and further research is being done to corroborate this working hypothesis. Previous research confirms the existence of the *O* phase for the PPT-composition BZT-0.5BCT at poling fields of 3–6 kV/cm by *in situ* x-ray diffraction [36], which supports a field-induced ferroelectric-ferroelectric phase transition in this material. As a consequence, we speculate that the *O* phase transition during poling occurs for compositions around the PPT area (BZT-0.4BCT, BZT-0.45BCT, and BZT-0.52BCT) and, therefore, a single-domain state in PPT BZT-*x*BCT corresponds to the orthorhombic phase. The electric-field-induced phase transition as a strain mechanism in the BZT-*x*BCT warrants further research. For instance, *in situ* x-ray or neutron-diffraction analysis at different electric-field values and orientations could potentially resolve the current working hypothesis [49].

The microstructure evolution in the BZT-*x*BCT system correlates well with the macroscopic data, reported in this study. Thus, maximum values in saturation and remanent polarization for PPT compositions [Figs. 2(a) and 2(b)) correspond to the miniaturization of domains. For instance, the higher coercive field for tetragonal BZT-0.6BCT [Fig. 2(c)] is correlated with the high poling fields required to induce the singe-domain state in comparison with rhombohedral and PPT compositions. Enhanced values of maximum and remanent strain for BZT-0.4BCT and BZT-0.52BCT compositions [Fig. 2(d) and 2(e)], which locate near to the (*R*-*O*) and (*O*-*T*) PPT areas in the phase diagram, respectively, coincide with reduction in the domain size. A sharp decrease in these values for the BZT-0.45BCT can be attributed to the presence of an orthorhombic structure far from phase boundaries.

In summary, domain evolution as a function of an applied electric field in lead-free BZT-*x*BCT piezoelectric ceramic is investigated. Transformations of a multiple-domain state $(A) \rightarrow$ nanodomain state $\rightarrow$ single-domain state occur for all studied compositions. Further increase in poling field leads to the multiple-domain state (*B*) formation, which can be associated with strain incompatibility between neighboring grains under the electric field. SAED patterns did not reveal any detectable changes during the poling process. Domain-wall motion during electrical poling is a sign of a high extrinsic contribution to the piezoelectric response in all studied lead-free BZT-*x*BCT compositions. Stresses are suggested to determine the domain-configuration evolution under the field.

ACKNOWLEDGMENTS

The *in situ* electric field TEM analysis was conducted at the Ames Laboratory, USA, for which we are grateful to Dr. Matthew Kramer and Dr. Lin Zhou for their assistance. We acknowledge Prof. Jürgen Rödel for helpful discussions. This work was supported by the Deutsche Forschungsgemeinschaft, Sonderforschungsbereich 595 and the ADRIA Hesse State Center for Adaptronics.

[1] B. Jaffe, W. R. Cook, and H. Jaffe, *Piezoelectric Ceramics* (Academic Press, New York, 1971).
[2] EU-Directive 2011/65/EU, Off. J. Eur. Union **L174**, 88 (2011).
[3] G. A. Smolenskii, V. A. Isupov, A. I. Agranovskaya, and N. N. Krainik, New ferroelectrics of complex composition, Sov. Phys. Solid State **2**, 2651 (1961).
[4] T. Takenaka, H. Nagata, Y. Hiruma, Y. Yoshii, and K. Matumoto, Lead-free piezoelectric ceramics based on perovskite structures, J. Electroceram. **19**, 259 (2007).
[5] G. O. Jones and P. A. Thomas, The tetragonal phase of $Na_{0.5}Bi_{0.5}TiO_3$: A new variant of the perovskite structure, Acta Crystallogr. Sect. B **56**, 426 (2000).
[6] L. A. Schmitt, J. Kling, M. Hinterstein, M. Hoelzel, W. Jo, H.-J. Kleebe, and H. Fuess, Structural investigations on lead-free $Bi_{1/2}Na_{1/2}TiO_3$-based piezoceramics, J. Mater. Sci. **46**, 4368 (2011).
[7] S.-T. Zhang, A. B. Kounga, E. Aulbach, and Y. Deng, Temperature-dependent electrical properties of $0.94Bi_{0.5}Na_{0.5}TiO_3$-$0.06BaTiO_3$ ceramics, J. Am. Ceram. Soc. **91**, 3950 (2008).

[8] W. C. Lee, Y. F. Lee, M. H. Tseng, C.-Y. Huang, and Y.-C. Wu, Crystal structure and ferroelectric properties of $(Bi_{0.5}Na_{0.5})TiO_3$-$Ba(Zr_{0.05}Ti_{0.95})O_3$ piezoelectric ceramics, J. Am. Ceram. Soc. **92**, 1069 (2009).

[9] S.-T. Zhang, A. B. Kounga, E. Aulbach, H. Ehrenberg, and J. Rödel, Giant strain in lead-free piezoceramics $Bi_{0.5}Na_{0.5}TiO_3$-$BaTiO_3$-$K_{0.5}Na_{0.5}NbO_3$ system, Appl. Phys. Lett. **91**, 112906 (2007).

[10] J. Rödel, W. Jo, K. T. P. Seifert, E.-M. Anton, T. Granzow, and D. Damjanovic, Perspective on the development of lead-free piezoceramics, J. Am. Ceram. Soc. **92**, 1153 (2009).

[11] Y. Saito, H. Takao, T. Tani, and T. Nonoyama, Lead-free piezoceramics, Nature (London) **432**, 84 (2004).

[12] W. Liu and X. Ren, Large Piezoelectric Effect in Pb-Free Ceramics, Phys. Rev. Lett. **103**, 257602 (2009).

[13] D. Xue, Y. Zhou, H. Bao, C. Zhou, J. Gao, and X. Ren, Elastic, piezoelectric, and dielectric properties of $Ba(Zr_{0.2}Ti_{0.8})O_3$-$50(Ba_{0.7}Ca_{0.3})TiO_3$ Pb-free ceramic at the morphotropic phase boundary, J. Appl. Phys. **109**, 054110 (2011).

[14] W. Wang, W. L. Li, D. Xu, W. P. Cao, Y. F. Hou, and W. D. Fei, Phase transitions in $(1-x)BaZr_{0.2}Ti_{0.8}O_3$-$xBa_{0.7}Ca_{0.3}TiO_3$ powders and ceramic pellets, Ceram. Int. **40**, 3933 (2014).

[15] M. Acosta, N. Novak, W. Jo, J. Rödel, and W. Jo, Relationship between electromechanical properties and phase diagram in the $Ba(Zr_{0.2}Ti_{0.8})O_3$-$x(Ba_{0.7}Ca_{0.3})TiO_3$ lead-free piezoceramic, Acta Mater. **80**, 48 (2014).

[16] P. Mishra and P. Kumar, Enhanced dielectric and piezoelectric properties of BZT-BCT system near MPB, Ceram. Int. **40**, 14149 (2014).

[17] J. Gao, X. Hu, L. Zhang, F. Li, L. Zhang, Y. Wang, Y. Hao, L. Zhong, and X. Ren, Major contributor to the large piezoelectric response in $(1-x)Ba(Zr_{0.2}Ti_{0.8})\times O_3$-$x(Ba_{0.7}Ca_{0.3})TiO_3$ ceramics: Domain wall motion, Appl. Phys. Lett. **104**, 252909 (2014).

[18] M. C. Ehmke, J. Glaum, M. Hoffman, J. E. Blendell, and K. J. Bowman, *In situ* x-ray diffraction of biased ferroelastic switching in tetragonal lead-free $(1-x)Ba(Zr_{0.2}Ti_{0.8})O_3$-$x(Ba_{0.7}Ca_{0.3})TiO_3$ piezoelectrics, J. Am. Ceram. Soc. **96**, 2913 (2013).

[19] M. Acosta, N. Khakpash, T. Someya, N. Novak, W. Jo, H. Nagata, G. A. Rossetti, and J. Rödel, Origin of the large piezoelectric activity in $(1-x)Ba(Zr_{0.2}Ti_{0.8})\times O_3$-$x(Ba_{0.7}Ca_{0.3})TiO_3$ ceramics, Phys. Rev. B **91**, 104108 (2015).

[20] D. E. Cox, B. Noheda, G. Shirane, Y. Uesu, K. Fujishiro, and Y. Yamada, Universal phase diagram for high-piezoelectric perovskite systems, Appl. Phys. Lett. **79**, 400 (2001).

[21] H. Bao, C. Zhou, D. Xue, J. Gao, and X. Ren, A modified lead-free piezoelectric BZT-xBCT system with higher T_c, J. Phys. D **43**, 465401 (2010).

[22] J. Gao, D. Xue, Y. Wang, D. Wang, and L. Zhang, Microstructure basis for strong piezoelectricity in Pb-free $Ba(Zr_{0.2}Ti_{0.8})O_3$-$(Ba_{0.7}Ca_{0.3})TiO_3$ ceramics, Appl. Phys. Lett. **99**, 092901 (2011).

[23] M. C. Ehmke, S. N. Ehrlich, J. E. Blendell, and K. J. Bowman, Phase coexistence and ferroelastic texture in high strain $(1-x)Ba(Zr_{0.2}Ti_{0.8})O_3$-$x(Ba_{0.7}Ca_{0.3})TiO_3$ piezoceramics, J. Appl. Phys. **111**, 124110 (2012).

[24] A. Bjørnetun Haugen, J. S. Forrester, D. Damjanovic, B. Li, K. J. Bowman, and J. L. Jones, Structure and phase transitions in $0.5(Ba_{0.7}Ca_{0.3}TiO_3)$-$0.5(BaZr_{0.2}Ti_{0.8}O_3)$ from −100 °C to 150 °C, J. Appl. Phys. **113**, 014103 (2013).

[25] F. Benabdallah, A. Simon, H. Khemakhem, C. Elissalde, and M. Maglione, Linking large piezoelectric coefficients to highly flexible polarization of lead free $BaTiO_3$-$CaTiO_3$-$BaZrO_3$ ceramics, J. Appl. Phys. **109**, 124116 (2011).

[26] D. S. Keeble, F. Benabdallah, P. A. Thomas, M. Maglione, and J. Kreisel, Revised structural phase diagram of $(Ba_{0.7}Ca_{0.3}TiO_3)$-$(BaZr_{0.2}Ti_{0.8}O_3)$, Appl. Phys. Lett. **102**, 092903 (2013).

[27] Y. Tian, L. Wei, X. Chao, Z. Liu, and Z. Yang, Phase transition behavior and large piezoelectricity near the morphotropic phase boundary of lead-free $(Ba_{0.85}Ca_{0.15})(Zr_{0.1}Ti_{0.9})O_3$ ceramics, J. Am. Ceram. Soc. **96**, 496 (2013).

[28] L. Zhang, M. Zhang, L. Wang, C. Zhou, Z. Zhang, Y. Yao, L. Zhang, D. Xue, X. Lou, and X. Ren, Phase transitions and the piezoelectricity around morphotropic phase boundary in $Ba(Zr_{0.2}Ti_{0.8})O_3$-$x(Ba_{0.7}Ca_{0.3})TiO_3$ lead-free solid solution, Appl. Phys. Lett. **105**, 162908 (2014).

[29] J. Gao, L. Zhang, D. Xue, T. Kimoto, M. Song, L. Zhong, and X. Ren, Symmetry determination on Pb-free piezoceramic $0.5Ba(Zr_{0.2}Ti_{0.8})O_3$-$0.5(Ba_{0.7}Ca_{0.3})TiO_3$ using convergent beam electron diffraction method, J. Appl. Phys. **115**, 054108 (2014).

[30] F. Bai, J. Li, and D. Viehland, Domain hierarchy in annealed (001)-oriented $Pb(Mg_{1/3}Nb_{2/3})O_3$-$x\%PbTiO_3$ single crystals, Appl. Phys. Lett. **85**, 2313 (2004).

[31] H. Wang, J. Zhu, N. Lu, A. A. Bokov, Z.-G. Ye, and X. W. Zhang, Hierarchical micro-/nanoscale domain structure in M_C phase of $(1-x)Pb(Mg_{1/3}Nb_{2/3})O_3$-$xPbTiO_3$ single crystal, Appl. Phys. Lett. **89**, 042908 (2006).

[32] H. Wang, J. Zhu, X. W. Zhang, Y. X. Tang, and H. S. Luo, Domain structure of adaptive orthorhombic phase in [110]-poled $Pb(Mg_{1/3}Nb_{2/3})O_3$-$30.5\%PbTiO_3$ single crystal, Appl. Phys. Lett. **92**, 132906 (2008).

[33] S. Zhukov, Y. A. Genenko, M. Acosta, H. Humburg, W. Jo, J. Rödel, and H. von Seggern, Polarization dynamics across the morphotropic phase boundary in $Ba(Zr_{0.2}Ti_{0.8})O_3$-$x(Ba_{0.7}Ca_{0.3})TiO_3$ ferroelectrics, Appl. Phys. Lett. **103**, 152904 (2013).

[34] M. Zakhozheva, L. A. Schmitt, M. Acosta, W. Jo, J. Rödel, and H.-J. Kleebe, *In situ* electric field induced domain evolution in $Ba(Zr_{0.2}Ti_{0.8})O_3$-$0.3(Ba_{0.7}Ca_{0.3})TiO_3$ ferroelectrics, Appl. Phys. Lett. **105**, 112904 (2014).

[35] F. Cordero, F. Craciun, M. Dinescu, N. Scarisoreanu, C. Galassi, W. Schranz, and V. Soprunyuk, Elastic response of $(1-x)Ba(Ti_{0.8}Zr_{0.2})O_3$-$x(Ba_{0.7}Ca_{0.3})TiO_3$ ($x = 0.45$–0.55) and the role of the intermediate orthorhombic phase in enhancing the piezoelectric coupling, Appl. Phys. Lett. **105**, 232904 (2014).

[36] H. Guo, B. K. Voas, S. Zhang, C. Zhou, X. Ren, S. P. Beckman, and X. Tan, Polarization alignment, phase transition, and piezoelectricity development in polycrystalline $0.5Ba(Zr_{0.2}Ti_{0.8})O_3$-$0.5(Ba_{0.7}Ca_{0.3})TiO_3$, Phys. Rev. B **90**, 014103 (2014).

[37] H. Guo, C. Zhou, X. Ren, and X. Tan, Unique single-domain state in a polycrystalline ferroelectric ceramic, Phys. Rev. B **89**, 100104 (2014).

[38] R. Schierholz and H. Fuess. Ferroelectric domains in PZT ceramics at the morphotropic phase boundary. Can the splitting of reflections in SAED patterns be used for the distinction of different pseudo-cubic phases?, J. Appl. Crystallogr. **45**, 766 (2012).

[39] J. Ricote, R. W. Whatmore, and D. J. Barber, Studies of the ferroelectric domain configuration and polarization of rhombohedral PZT ceramics, J. Phys. Condens. Matter **12**, 323 (2000).

[40] M. Tanaka and G. Honjo, Electron optical studies of barium titanate single crystal films, J. Phys. Soc. Jpn. **19**, 954 (1964).

[41] Y. H. Hu, H. M. Chan, Z. X. Wen, and M. P. Harmer, Scanning electron microscopy and transmission electron microscopy study of ferroelectric domains in doped $BaTiO_3$, J. Am. Ceram. Soc. **69**, 594 (1986).

[42] K. Evans and R. Beanland, High dynamic range electron imaging: The new standard, Microsc. Microanal. **20**, 1601 (2014).

[43] M. E. Lines and A. M. Glass, *Principles and Applications of Ferroelectrics and Related Materials* (Clarendon Press, Oxford, 2001).

[44] G. A. Rossetti, A. G. Khachaturyan, G. Akcay, and Y. Ni, Ferroelectric solid solutions with morphotropic boundaries: Vanishing polarization anisotropy, adaptive, polar glass, and two-phase states, J. Appl. Phys. **103**, 114113 (2008).

[45] S. Schaab and T. Granzow, Temperature dependent switching mechanism of $(Pb_{0.92}La_{0.08})(Zr_{0.65}Ti_{0.35})O_3$ investigated by small and large signal measurements, Appl. Phys. Lett. **97**, 132902 (2010).

[46] R. Theissmann, L. A. Schmitt, J. Kling, R. Schierholz, K. A. Schönau, H. Fuess, M. Knapp, H. Kungl, and M. J. Hoffmann, Nanodomains in morphotropic lead zirconate titanate ceramics: On the origin of the strong piezoelectric effect, J. Appl. Phys. **102**, 024111 (2007).

[47] G. Tutuncu, B. Li, K. Bowman, and J. L. Jones, Domain wall motion and electromechanical strain in lead-free piezoelectrics: Insight from the model system $(1-x)Ba(Zr_{0.2}Ti_{0.8})O_3$-$x(Ba_{0.7}Ca_{0.3})TiO_3$ using *in situ* high-energy x-ray diffraction during application of electric fields, J. Appl. Phys. **115**, 144104 (2014).

[48] M. Hinterstein, M. Knapp, M. Holzel, W. Jo, A. Cervellino, H. Ehrenberg, and H. Fuess, Field-induced phase transition in $Bi_{1/2}Na_{1/2}TiO_3$-based lead-free piezoelectric ceramics, J. Appl. Crystallogr. **43**, 1314 (2010).

[49] M. Hinterstein, J. Rouquette, J. Haines, P. Papet, M. Knapp, J. Glaum, and H. Fuess, Structural Description of the Macroscopic Piezo- and Ferroelectric Properties of Lead Zirconate Titanate, Phys. Rev. Lett. **107**, 077602 (2011).